General trends between solute segregation tendency and grain boundary character in aluminum - an ab inito study

Reza Mahjoub[a]*, Kevin J. Laws[b], Nikki Stanford[a], Michael Ferry[b]
a) Future Industry Institute, University of South Australia, Mawson Lakes SA 5095, Australia
b) School of Materials Science and Engineering, The University of New South Wales (UNSW Sydney), Sydney, NSW 2052, Australia

ABSTRACT

Quantum mechanical calculations have been performed to establish general trends in propensity for the segregation of solutes across the periodic table at or in the neighborhood of an extended set of commonly observed special grain boundaries in face centered cubic aluminium. To this end, Al has been considered as the matrix and elements from 3d and 4d transition metals as well as those from group II, III and IV have been selected as solute atoms. For transition metal solutes, we find a concave-up parabolic-like dependency of segregation energy as a function of atomic number that is argued to be caused by the competition between chemical bonding and atomic size effects. The analysis is corroborated quantitatively by the computation of crystal orbital Hamiltonian population for solute-Al and Al-Al pairs as well as the Voronoi polyhedral surrounding solutes at a sample GB. The parabolic-like (concave-down trend) dependency of the cohesiveness of grain boundaries is explained by a similar trend in the bonding strength of Al-Al pairs at the segregated GBs. We extend this investigation to examine the stability of the solid solution polycrystalline state by comparing the calculated segregation energy against the combined energetic cost of grain boundary and intermetallic precipitate formation. The results may serve as a design tool for tailoring polycrystalline alloys with desired properties.

---

* Corresponding author, electronic mail: reza.mahjoub@unisa.edu.au

1. Introduction

The properties of a crystalline material, whether it is a metal, intermetallic compound or ceramic etc., can be significantly altered by the presence of point, line and surface defects [1, 2]. A major surface (2D) defect is the grain boundary (GB), characterized by five macroscopic degrees of freedom consisting of the rotation axis, the normal to the interface plane and the rotation angle [3]. Hence, the arrangement and bonding between atoms in the vicinity of a GB and, hence, its energetic state, is expected to be much different to the interior of the adjacent grains (hereafter termed bulk) [4]. As such, the shape and topology intimately affect critical mechanical and physical properties, as well as other properties such as corrosion susceptibility [1, 5]. Indeed, the concept of grain boundary engineering (GBE) [6], aimed at optimizing the structure and properties of the GBs in a material for a particular application, is an important method for designing polycrystalline alloys with improved properties [6, 7].

Grain boundaries are thermodynamically unstable structural defects since the energetic cost of boundary formation cannot be recompensed by their relatively low entropic contribution to free energy [8]. Hence, for a given polycrystal, a reduction in grain size results in an increase in total GB area and, hence, stored energy. If the grain size is reduced to the nano-scale (submicron), the grain boundary energy becomes so large that the driving force for grain coarsening may approach the energies associated with in some solid-state phase transformations [9]. Hence, fine grained structures are inherently unstable.

The addition of certain alloying elements to a metal is one of the most effective ways in altering the local structure and chemistry of GBs [6]. The spatial distribution of solutes is often disrupted by the presence of GBs, whereby certain atom species tend to segregate to these defects due to different energetic states [4]. Hence, GB segregation may have a significant influence on the: (i) stability of a microstructure against grain coarsening [10], and (ii) cohesive

strength of a given type of GB, which may lead to either strengthening or embrittlement. Both of these outcomes are affected by factors such as the type and amount of solute, GB character, operating temperature of the material etc. [11]. Indeed, there are numerous reported examples of solute engendered grain size stability and GB embrittlement in metals and alloys [1, 12]. For example, Oxygen segregation to GBs in nanocrystalline Al stabilizes the microstructure from coarsening, increases strength but reduces ductility [13], and GB segregation of Zr in nanocrystalline Pd also stabilizes the microstructure [14, 15]. It is well-known that GB segregation of Ga in polycrystalline Al [16] results in a loss of boundary cohesion and subsequent embrittlement [17].

However, it is difficult to measure directly the effect of solute segregation on important features such as interfacial energy along different orientations and the resultant changes in the chemical environment at a boundary [1]. As a result, ab initio studies of GB segregation has been used extensively to shed light on the microscopic features of intergranular brittle fracture which is known to be among the most perilous deficiencies of structural materials [12]. Using first principles, Olson and co-workers calculated a large driving force for segregation of Na solutes to a symmetrical tilt boundary ($\Sigma5(012)[100]$) in Al, showing that the resulting cohesiveness of the boundary is reduced markedly [18]. These workers also showed that, while Zn atoms also have a large driving force for segregating to the same type of GB, the outcome was weak embrittlement since in the GB region, the bonding charge density along the Zn-Al bonds is slightly reduced rendering them weaker than Al-Al bonds [11]. The same GB was studied by Zhao et al. [19] and it was found that segregation driving force of Cu impurities is larger than Mg and while Mg segregation results in embrittlement of the GB, Cu segreagants enhance its cohesion [19]. Most ab initio studies of GB segregation have been confined to certain types of solute atoms and grain boundaries. In an attempt to construct a phenomenological model of cohesion of segregated GBs, Geng et al. [19] investigated the effect of Mo, Pd, Co, Ru, W and

Re on segregation to the Σ3(111)[100] boundary in Fe. More recently, Wu et al. investigated the segregation of six types of transition metal (TM) atom, each from the 5th and 6th rows of the periodic table, to eight types of symmetrical tilt boundaries in body centered cubic tungsten. It was shown that the cohesiveness of segregated boundaries shows a similar shape with increasing atomic number (Z) for a given type of TM atom with 4d and 5d orbitals [20]. They also showed that, while strongly embrittling TM atoms draw charge from the host atoms, removing it from the bonds holding the boundary together [21], the atomic size of the solute also plays an important role in the GB decohesion [20]. Hence, significant relocation of atoms near the GB may be introduced by segregated solutes implying the importance of atom or volume size effect of solutes on the physical and mechanical properties of GBs [22]. This effect is associated with a strain energy that may be approximated as a function of changes in the atomic volumes of solute and solvent as well as their bulk and shear moduli [22].

While these foregoing studies are rigorous, we currently lack a more comprehensive first principles study of GB segregation effects addressing a broader range of properties, including the driving force for segregation and phase stability, and involving a wide range of solute types segregating to GBs exhibiting a variety of characters. These are more computationally expensive studies, but are needed for recognizing and explaining general trends at the atomic level, thereby leading to more fundamental predictions of structure-property relationships in engineering materials [23].

In the present work, extensive DFT calculations were carried out to shed light on the general trends in the energetic properties of a large set of solutes across the periodic table (comprising three atoms from group II, five atoms from groups III and IV, and TMs from the 4th and 5th periods) segregating to special GBs in face centered cubic (FCC) metals such as aluminum. It is worth noting that experimental measurements in polycrystalline Al have revealed [24] that while the most populated grain boundary orientations are (111) and (113), boundaries

terminating on higher index planes such as symmetric [110] tilt GBs are relatively highly populated [24] and their distribution is inversely related to GB energies [24]. It is also pertinent to note that to render computationally expensive ab inito calculations feasible, a limited number of atoms in the simulation cell needs to be used. As such, we consider an extended set of symmetric tilt GBs observed in Al, spanning a wide range of topological aspects such as misorientation angle, planar coincidence site lattice (CSL) density (Σ) and interplanar spacing [25].

We analyze the local electronic structure at sample GBs, by calculating the projected density of states (pDOS), and quantitatively describe chemical bonding by projected crystal orbital Hamiltonian population (pCOHP) [26-30], which gives the population of bonding or antibonding states for a given pair of atoms. The integral of pCOHP (denoted as ICOHP) can be interpreted as the level of covalency of atomic bonding.

We explain these energetic trends in terms of the cooperative and competitive relationship between chemical bonding and strain energy due to the size effect of solute atoms.

2. Computational method

First principles calculations based on DFT were carried out to calculate the interfacial energy of twelve symmetric high angle tilt GBs observed in FCC Al [25] as well as the energetic effects associated with the addition of solute atoms from group II, III, IV and 3d and 4d transition metals (TM) of the periodic table. Vienna ab initio software package was used [31] implementing the projector augmented wave method to represent the combined potential of core electrons and nuclei [32]. The Perdew–Burke–Ernzerhof gradient approximation is implemented to represent the exchange-correlation functional [33]. A cut-off energy of 390 eV

was chosen for the plane wave basis and the self-consistent electronic optimization was converged to 10^{-7} eV. Each GB is represented by a supercell containing two misoriented slabs with a vacuum layer of 10 A° on top. The schematic depiction of the studied GBs is provided in Figure S1 [34] of the supplementary materials and the tilt axis, misorientation angle, the number of atoms in the supercell and supercell dimensions are given in Table 1. The GBs include both [110] and [100] tilt axes and (111) and (113) boundary orientations which are considered highly populated in Al by experimental measurements [24]. They span a wide range of misorientation angle, planar coincidence site lattice (CSL) density (Σ) and interplanar spacing. While periodic boundary conditions were applied in three dimensions, the vacuum layer prevents interference from the out of plane images due to periodic boundary conditions [11, 18, 35-37]. The mesh of Γ-centered k-points to sample the Brillouin zone were chosen such that their density is less than 0.032 $A^{\circ -1}$. While the thickness of each layer is considered sufficiently large, i.e. greater than or equal to 30 A°, tests were performed to ensure that an effective convergence is attained with respect to the thickness of slabs, the vacuum layer and the density of k-points [38].

The excess ground state energy of a GB-containing system over that of a system with a free surface (FS) represented by a supercell containing a misoriented slab and a vacuum layer [4, 11, 35], indicates GB energy (γ_{GB}) and can be expressed as [35, 39]:

$$\gamma_{GB} = (E_{GB} - E_{FS})/S \quad (1)$$

where E_{GB} and E_{FS} are the energies of the supercell containing the GB and the free surface (FS), respectively and S is the GB area. The work of separation (W_{sep}), defined as the reversible work needed to separate the GB into two free surfaces [40] and the free surface energy (σ) respectively, are calculated as [35, 40, 41]:

$$W_{sep} = 2\sigma - \gamma_{GB} \quad (2)$$

$$\sigma = (E_{FS} - \frac{N_{FS}}{N_{Bulk}} E_{Bulk})/2S \quad (3)$$

In equations (2) and (3), E_{Bulk} is the structure's bulk energy whilst N_{FS} and N_{Bulk} indicate the number of atoms contained in the supercell representing the slab and the bulk, respectively.

As bonding at GBs is different from the bulk, solutes may segregate to GBs to reduce interfacial energy. This energetic deficit is represented by segregation energy and is given as [4]:

$$E_{seg}^{S} = (E_{GB}^{S} - E_{GB}) - (E_{Bulk}^{S} - E_{Bulk}) \quad (4)$$

where E_{GB}^{S} and E_{Bulk}^{S} are the ground state energies of the supercell containing the GB with a segregated solute and the bulk crystal with a solute atom, respectively. As such, the higher the E_{seg}^{S}, the lower the tendency of a solute to segregate to a GB.

It is pertinent to note that the binding energies of a mobile solute to a GB or a free surface can be calculated as $E_{b,X}^{S} = E_{X}^{S} - (E_{X} - E_{atom}^{S})$ where X represents GB or an FS and E_{atom}^{S} is the atomic energy of the solute [11]. While a deficit in $E_{b,GB}^{S}$ with respect to $E_{b,FS}^{S}$ indicates that the GB is favored over a surface appearing in a stress-induced crack, a surplus energy implies the propensity for crack growth due to interfacial embrittlement by solute segregation. As such, the embrittling potency, which is a quantitative indicator for the segregation-induced interfacial embrittlement and defined as the difference between $E_{b,GB}^{S}$ and $E_{b,FS}^{S}$, can be calculated as [11, 42]:

$$\Delta E = (E_{GB}^{S} - E_{GB)} - (E_{FS}^{S} - E_{FS}) \quad (5)$$

3. Results

The calculated γ_{GB}, W_{sep} and σ for the GBs are given in Table 1 and depicted as functions of misorientation angle in Figure S2 of the supplementary materials. The smallest and largest γ_{GB} correspond to Σ3[110](111) and Σ17[100](410), respectively, and no clear correlation can be seen between γ_{GB} and Σ (the reciprocal density of coincident lattice sites) or misorientation angle. However, γ_{GB} as the energy barrier to form a homophase interface tends to correlate inversely with W_{sep}.

Aluminum belongs to group III of the periodic table with an outer electron configuration $3s^2 3p^1$ (valence electrons) and for possible solute atoms, we have considered a set of 28 elements comprising three elements from group II (i.e. Mg, Ca and Sr), four elements from groups III and IV (i.e. Ga, In, Si, Ge and Sn) and all 3d and 4d transition metals (TM).

Up to four substitutional sites at a given GB or in the atomic planes close to it are specified for substitutional solute atoms, which are marked in Figure S1. As such, for a given solute atom, the segregation energy at 41 different sites has been calculated and provided in Table SI of the supplementary materials. Figure 1 shows the segregation energy landscape as a function of solute atomic number (Z_{solute}). Embrittling potency has been computed and Figure 2 depicts it as a function of Z_{solute} for the sites that correspond to a negative segregation energy, indicating they are energetically favored positions over the bulk.

In order to gain a more in-depth insight at the microscopic scale into the effect of solute segregation to GBs, the atomic configuration, electronic structure and chemical environment in the vicinity of the solute segregated Σ5[001](210) have been investigated.

First, the atomic configuration was tessellated to find Voronoi polyhedra formed by the nearest neighbors of a central atom [43, 44] and, in particular, the solute segregated to the GB. The volume of Voronoi cell containing the solute was calculated and depicted in Figure 3 as a function of the type of solute segregant.

Next, the electronic structure of Σ5[001](210) was studied and supplementary Figure S3 shows the pDOS of a sample of two types of solute segregant. It is pertinent to note that the analysis of the pDOS of TMs indicates strong spd hybridization. While the qualitative features of pDOS of TM-containing alloys are similar to those observed in their constituent elemental metals, the changes in the location of the d band with respect to E_F can be of marked significance [45] since it reflects the stabilizing or destabilizing effect of bonding or antibonding electronic states, respectively [46, 47].

As such, this study has been extended to include the calculation of -pCOHP and -ICOHP of Al-solutes segregated to the GB. The positive or negative value of -COHP indicate bonding or antibonding states, respectively, and the mean of -ICOHP at the Fermi level (E_F) can be interpreted as the level of covalency of atomic bonding. Supplementary Figure S3 illustrates them as a function of energy for a sample of two solutes, consisting of Sc and Ni segregated at the GB. The calculated values of <-pCOHP> and <-ICOHP> for Al-segregant pairs are depicted in Figure 4 and listed in supplementary Table SIII.

To better understand the atomic bonding in the vicinity of the GB, charge distribution was calculated for all 28 solute segregants and Figure 5 provides charge density in the GB vicinity for a sample of five solutes consisting of Mg, Sn, Ni, Cu and Pd. This leads the way to the calculation of -ICOHP for a neighboring Al-Al pair close to the boundary, which is depicted in Figure 6 as a function of different solute segregants.

Finally, solute segregation energies are used to create a map for the stability of polycrystalline phase in the solid solution as provided in Figure 7.

4. Discussion

The segregation energy landscape, shown in Figure 1, spans a rather wide range of energies for a given solute and, hence, may be regarded as a random variable to facilitate extracting conclusions. We begin with the solutes of group II (Figure 1(a)) and observe that as Z_{solute} increases, the segregation energy decreases, indicating that there is an increasing tendency of solute atoms to leave the bulk environment and segregate to the GBs. This trend can be seen clearly in the average of the segregation energy for a given solute as well as the minimum values of E_{seg}^{S}. The same trend can be observed in solutes of group III (i.e. Ga and In) and Ge and Sn of group IV. On the whole, in each group, the larger the atomic number, the higher the segregation tendency and group II atoms seem to show more propensity for segregation than those of group III and IV.

The variation of E_{seg}^{S} with respect to Z_{solute} of 3d transition metals (TM) seems more complicated and follows a concave-up parabolic-like dependency which is distorted at the right end (Figure 1(b)). Moving to the right of the periodic table, E_{seg}^{S} tends to increase slightly and peaks at V where it begins to decrease to its minimum at Co and Ni. The upward trend resumes for Cu and continues, albeit to a lesser degree, to Zn. As for 4d-TM solutes, while E_{seg}^{S} exhibits a similar trend, the range of segregation energies spanned by 4d-TMs solutes is widened and relatively more negative or positive values for E_{seg}^{S} are observed. On the whole, the driving force to segregation seems to be stronger for late TMs in particular those of columns 9 and 10.

Now, it is worth comparing E_{seg}^{S} and ΔE of solutes segregated to Σ5[001](210) with bonding strength at the GB as well as solute volume size [22] approximated by Voronoi cell volume, and the strain energy associated to it.

4.1 Segregation, GII, III, IV

Beginning with group II solutes, the bonding strength, represented by <-ICOHP> and shown in Figure 4(a) increases as Z_{solute} is increased. This trend correlates with the decrease in E_{seg}^{S} and the increase in segregation driving force depicted in Figure 4(c). While similar correlation is observed for group III solutes, <-ICOHP> for group IV solutes shows mixed results as Z_{solute} increases (i.e. it decreases from Si to Ge and increases from Ge to Sn). However, the increase in Z_{solute} of group IV solutes for Si, Ge and Sn correlates with the decreases of their Voronoi cell volume at the GB from 44.2 to 41.3 and 30.2 $A^{\circ 3}$, respectively, as shown in Figure 3(a). The strain energy associated with the solute Voronoi cell volume contributes to both E_{GB}^{S} and E_{Bulk}^{S}, and revisiting equation (4), the change in E_{seg}^{S} is a function of the difference between E_{GB}^{S} and E_{Bulk}^{S}. It is worth noting that the increase in Z_{solute} of group IV solutes coincides with a decrease in the Voronoi cell volume in the bulk (i.e. from 8.6 to 9.4 and 11.9 $A^{\circ 3}$ for Si, Ge and Sn, respectively). The net difference in Voronoi cell volume at the GB and in bulk decreases from 35.5 to 31.9 and 18.3 $A^{\circ 3}$ for Si, Ge and Sn, respectively. This indicates a similar decrease in the net contribution of strain energy to E_{seg}^{S}, which is well reflected in the decrease of segregation energy, i.e. the increase of the driving force for segregation (Figure 4(c)).

4.2 Segregation, TMs

Figure 4(d) shows that E_{seg}^{Sc} is relatively small and the driving force for Sc to segregate to the GB is relatively large. The driving force begins to decline as one moves towards Mn, then increases for Fe, Co and Ni, slightly decreases for Cu and increases again for Zn. Indeed, for early 3d-TMs, both relatively small Voronoi volume (Figure 3(b)) and large <-ICOHP> (Figure 4(b)) favour lower E_{seg}^{S}, i.e. stronger segregation driving force (Figure 4(d)). However, the Voronoi volume begins to nearly double for Cr and continues to increase for Mn and Fe. Then it smoothly decreases for Co, Ni and Cu and reduces for Zn. This decreasing trend in volume

and the associated strain energy is concurrent with the decrease in E_{seg}^{S} (i.e. the increase of segregation driving force). The slight increase of E_{seg}^{S} for Cu relative to Ni can be explained by comparing <-COHP> of Al-Cu and Al-Ni pairs in the bulk and at the GB (Table SIII). For Al-Cu, <-COHP> becomes negative (i.e. more unstable) as it moves from bulk to GB (0.001051 vs. -0.001124 per bond) whereas for Al-Ni, <-COHP> becomes less negative (i.e. more stable) as it moves from bulk to GB (-0.006352 vs. -0.002122 per bond).

As for 4d-TMs, a similar cooperative and competitive relationship between <-ICOHP> and solute volume can be observed. Figure 4(e) depicts a steep increase in E_{seg}^{S} from Y to Mo which can be correlated to the decline of <-ICOHP> (Figure 4(b)) for the same segregants. However, segregant volume begins to increase for Mo and peaks at Rh and concurrently, E_{seg}^{S} peaks smoothly at Tc and then slightly decreases for Ru. Finally, E_{seg}^{S} reduces more steeply to Cd, which can be correlated with the decrease of corresponding solute volume (Figure 3(b)).

It is worth noting that while the large increase in Voronoi volume of middle-to-late 3d-TM solutes is not only concurrent with considerable atomic relocation, but also the local charge distribution and chemical environment are markedly more altered for Fe, Co and Ni than other solutes (Figure 5).

4.3 Embrittlement

Figure 2 shows the embrittling potency landscape of solutes segregating into different positions at or in the vicinity of the studied symmetric tilt GBs. It is seen that while solutes from group II have both cohesive and embrittling effects on GBs, as one moves down the second column and Z_{solute} increases, the range of embrittling potency (ΔE) widens and covers both more positive and negative values. However, the average value of ΔE is slightly negative for Mg and Ca, indicating a weakly cohesive effect, and becomes slightly positive for Sr, implying it is a

weak embrittler [11]. A similar trend can be seen for group III and IV solutes, where increasing Z_{solute} correlates well with increasing embrittlement. As for TMs, ΔE depicted in Figure 2(b-c), is seen to have a parabolic dependency (concave-down trend) on Z_{solute}. This notion is consistent with prior theoretical and experimental investigations on the embrittlement potency of TM-segregated GBs in Ni and Fe systems [12, 48].

4.4 Embrittlement, GII, III, IV

To obtain further insight, ΔE of solutes segregated to Σ5[001](210) may be analyzed along with the charge distribution in the vicinity of the GB and the strength of neighboring Al-Al bonds across the boundary.

Starting with group II solutes, the charge density near a Mg segregated GB is shown in Figure 5(a). It is observed that the charge density between Al atoms of the two grains located close to the boundary is reduced markedly and the bonding is expected to be weak. To quantify the effect of different solute segregants on the strength of bonding, the -ICOHP between the pair of neighbouring Al atoms on two grains forming the GB and marked by "*x*", is calculated and provided in Figure 6(a). Moving down column II of the periodic table results in a weakening of bonding strength, with a concurrent increase in ΔE, as shown in Figure 6(c). The same correlation holds between the increasing embrittlement potency of solutes of group III and IV (Figure 6(a)) and the decreasing bond strength presented quantitatively by -ICOHP in Figure 6(c).

4.5 Embrittlement, TMs

The effect of the type of 3d-TM segregant on ΔE at Σ5[001](210) is given in Figure 6(d). Boundary cohesiveness increase slightly (i.e. ΔE decreases) as one moves from Sc to V, then

decreases (i.e. ΔE increases) from Cr to Cu and then slightly recovers for Zn. This trend correlates well with the bonding between the pair of neighbouring Al in the two grains forming the GB, as quantified by –ICOHP, Figure 6(b). It is worth noting that the pair of neighboring Al atoms on two grains forming the GB is different for the case of Fe, Co and Ni, from other solutes. This can be explained by comparing the charge density of a Ni-segregated GB shown in Figure 5(c) with those of Figure 5(a-b and d-e) where GBs are segregated with Mg, Sn, Cu and Pd, respectively. While the pattern of atomic configuration and respective charge density for the case of Cu is similar to that of Mg and indeed other solute atoms studied herein, the relocation of atoms near the GB and the resulting charge distribution is markedly different for Ni as well as Fe and Co. Therefore, the Al pair considered for calculating -ICOHP in the case of Ni segregating to the GB (Figure 5(c)) is different to that of Al pairs in other segregation cases (as shown in Figure 5(a,b,d and e), and thereby the -ICOHP as a function of 3d-TMs seems discontinuous for Fe, Co and Ni as shown in Figure 6(b).

While ΔE as a function of 4d-TMs exhibits quite a similar pattern to 3d-TMs, the -ICOHP of neighboring Al pair as a function of 4d-TM solutes remains continuous. Indeed, the pattern of atomic relocation near the GB due to solute segregation and the charge distribution associated with it stays almost the same for all 4d-TMs (e.g. Figure 5(e)).

Indeed, unlike 3d TMs, the valence electrons of TMs in the 4^{th} row of the periodic table are shielded and screened by the core 3d band [45]. As a result, 4d-TM valence electrons are less responsive to perturbations caused by hybridization with Al matrix valence electrons and their segregation behavior seems more dependent on the chemical environment provided by a given GB.

4.6 Polycrystalline phase stability

The segregation energy not only represents the tendency of a solute atom to segregate to a GB but also can be associated with the change in GB energy (γ_{GB}) through blending Gibbs adsorption isotherm ($d\gamma_{GB} = -\Gamma_s d\mu_s$, where Γ_s and μ_s are solute excess in the vicinity of a GB and solute chemical potential, respectively) with Langmuir-McLean isotherm, which governs the solute concentration in the crystal lattice and GB [8, 49]. This relation was first derived by Weissmuller for dilute solutions and is expressed as [10]:

$$\gamma_{GB} - \gamma_0 = \Gamma_s \left(RTln\left(\frac{n_s}{N_{LS}}\right) - E_{seg}^{S} \right) \quad (6)$$

where γ_0, n_s, N_{LS}, R and T are the GB energy of solute free crystalline structure, the number of solutes at the GB, the number of lattice sites at the GB, the ideal gas constant and absolute temperature, respectively.

Rearranging equation (6) and defining $E_{seg}^{S*} = -E_{seg}^{S}$ (so as to have a positive value for solute enrichment at GBs), provides a criterion for the stability of the GBs against grain growth, i.e. $E_{seg}^{S*} > \frac{\gamma}{\Gamma_s} - RTln\left(\frac{n_s}{N_{LS}}\right)$ [50, 51] stipulating that combined GB enthalpic penalty (first term on the RHS) and solid solution entropic contribution (second term on the RHS) should be surmounted by segregation energy. In an attempt to include the intermetallic precipitate formation at GBs, Schuh and co-workers considered the GB segregated state as a two-dimensional compound and expanded the foregoing criterion as [51]:

$$E_{seg}^{S*} > k\gamma + \Delta H_{mix} - \frac{1}{x_s^C}\Delta H_{form} \quad (7)$$

where k, ΔH_{mix}, ΔH_{form} and x_s^C are the scaling factor converting the GB energy unit from energy per area to energy per atom, mixing enthalpy, formation enthalpy of the intermetallic phase and the concentration of the solute atoms in the ordered compound, respectively.

It is worth noting that ground state segregation energy provided in DFT calculations can be approximated as segregation enthalpy [12, 52] since in solids, segregation volume is small [52] and the product of the segregation volume and pressure becomes negligible. The same approximation may be applied at ground state for mixing and formation enthalpies [51] and mixing energy (ΔE_{mix}) and formation energy (ΔE_{form}) obtained by DFT calculations.

Equation (7) stipulates that to stabilize a given GB with solutes, the segregation energy has to be large enough to recompense the combined GB energy (first term on the RHS) and the energy deficit due to the formation of an intermetallic compound (second and third terms on the RHS). For positive values of mixing energy, compound formation energy is considered as zero [50]. It is pertinent to note that if the solute segregation energy at a given GB overcomes only the GB energetic penalty (i.e. $k\gamma$), but falls short of compensating the energy deficit caused by compound formation, then the GB is considered metastable, i.e. as the temperature rises, the grains begin to grow. Based on equation (7) a stability map can be created where the abscissa represents the energetic deficit due to compound formation ($\Delta E_{mix} - \frac{1}{x_s^C}\Delta E_{form}$) and the ordinate shows E_{seg}^{S*}.

Figure 7 depicts the stability map for solute atoms segregated at or in the vicinity of twelve different GBs and the data for compound formation is adopted from Open Quantum Materials Database [53], as listed in Table SIV. It is noteworthy that the largest calculated value of γ_{GB} in pure FCC Al is used on the stability map to determine the borders between stable, metastable and unstable regions.

Figure 7(a-b) shows that solutes of group II, III and IV studied herein are located close to the origin of abscissa due to positive mixing energies. As a result, while a considerable number of GBs segregated by these solutes are stabilized against grain growth, they may suffer from embrittlement, in particular, as Z_{solute} increases (Figure 2).

On the other hand, a wave-like pattern can be seen for the location of 3d TMs on the abscissa of the stability map as shown in Figure 7(e). The early 3d TMs, Sc and Ti are pushed to the right of abscissa due to markedly stable intermetallic precipitate phases (i.e. $ScAl_2$ and $TiAl_2$), whereby the segregation energy can barely overcome both the compound formation and GB energies, resulting in a very large number of metastable homophase interfaces and leaving a small minority in the stable region. Moving to the right of the periodic table, the compound energetic deficit begins to decrease and, hence, middle 3d TMs retreat relatively to the left of abscissa where for an increasing number of GBs, segregation energy surmounts the relatively less stable compound formation energy (entries for Fe, Cr and Mn in Table SIV). Further to the right of periodic table, the late 3d TMs, i.e. Co and Ni form more stable compounds with solvent Al such as AlCo and AlNi, respectively, and as a consequence, more segregated GBs are found in the metastable region. For Cu with almost filled d band, the intermetallic AlCu becomes less stable with respect to all preceding TMs and thus it is pushed considerably to the left of abscissa where a larger number of stable segregated boundaries can be observed. For Zn with a completely filled and highly localized d band, no compound can be formed with Al and the mixing energy becomes positive. Therefore, Zn is pushed far left toward the origin of the stability map, close to non-TM solutes where a large number of segregated GBs are stable.

While a similar wave-like pattern can be observed for 4d TMs location on the abscissa of the stability map (Figure 7(f)), they are shifted relatively to the right of abscissa due to more stable compounds they form with Al (Table SIV). As a result, segregation energy of early to late 4d TMs fails to overcome the combined energetic cost of GB and compound formation and the vast majority of segregated boundaries are either metastable or unstable. Similar to Cu, the 4d band of Ag is almost filled and the stability of $AlAg_3$ markedly decreases with respect to other TMs, thereby pushing it far left toward the origin of abscissa and the number of segregated

GBs found in the stable region increases. Cd has a completely filled 4d band and behaves similar to Zn on the stability map.

4.7 Statistical analysis

The stability map shown in Figure 7 displays a set of points for each solute, corresponding to different STGBs. The fraction of points associated with a solute and located in the three regions of the map (as depicted in Figure S4) may point towards the formation probability of stable, metastable and unstable solute segregated GBs. However, while this approach does not take into account the population or the frequency of occurrence of specific GBs [24, 54], thorough experimental observations have shown that an inverse correlation exists between a GB population and its energy (γ_{GB}) [24, 54, 55]. Indeed, the GBs are indiscriminately high-energy regions in a polycrystalline material that increase the free energy with respect to the single crystalline phase [56] and, therefore, from a thermodynamic point of view, the lower the γ_{GB}, the easier and the more possible for the GB to form. To provide a more realistic statistical analysis of the stability of polycrystalline phase as a function of Z_{solute}, the inverse correlation between γ_{GB} (as listed in Table 1) can be used to introduce $w_i = \gamma_{GB,i}^{-1} / \sum_i (\gamma_{GB,i}^{-1})$ (i =1…12) as the weight factor affecting the abundance of STGBs in the solid solution. The weighted fraction of solute segregated GBs located in regions of stability, metastability and instability for a given solute is given in Figure 8 and can be regarded as the approximate propensity of a certain solute to render the polycrystalline phase stable, metastable or unstable.

It is seen that while the weighted fraction ratio (WFR) of stable segregated STGBs to unstable ones is noticeably small for most TMs, it is significantly larger for group II, III and IV solutes, in particular Sr followed by Mg, Si and Ca. However, stable to unstable WFR remains relatively high for solutes with almost filled and filled d-shells, i.e. Cu and Zn followed by Ag and Cd (column 11 and 12 of periodic table respectively). On the other hand, metastable to

unstable WFR of segregated STGBs are markedly larger for most TM solutes than for those of group II, III and IV, in particular Cu followed by Y and then Ni, Co and Fe. It is pertinent to note that apart from TM solutes of column 11 and 12, the weighted fraction of stable Fe, and to a lesser degree Mn segregated STGBs is relatively significant.

5. Concluding summary

First principles calculations in the context of DFT have been carried out to determine the segregation energy of 28 solutes across the periodic table at, or in the vicinity, of an extended set of commonly observed special GBs in FCC Al. The segregation energy is then used to find the embrittling potency indicating the mechanical behaviour of the segregated GBs. It is found that for transition metal solutes, segregation energy dependence on Z_{solute} is concave-up, parabolic-like, but the embrittling potency dependency on Z_{solute} is concave-down parabolic-like. Such trends are caused by the competition between size effects and chemical bonding where Al valence electrons hybridize with the d band of the TM solutes. For early TMs, where E_F is located close to the bottom of the d band populated with strong bonding states, decreasing strain energy determines the preference of the solutes to remain in the bulk over segregating to GBs. Moving to the right of the periodic table, the number of d electrons increases and E_F is progressively shifted towards the top of the d band where antibonding states become abundant. However, this effect seems to be overwhelmed by the effect of decreasing atomic size and leads to a driving force for the solutes to leave the bulk and segregate at or near GBs. The mechanical behaviour of segregated GBs is represented by embrittling potency and exhibit parabolic-like (with concave-down) trend. This correlates with the similar pattern of <-ICOHP> of Al-Al pairs in the solute segregated GBs and shows that enhancement of matrix bonds due to solute segregation is the key to GB cohesion. The analysis is expanded to the stability of the solid

solution polycrystalline state where we compare the calculated segregation energy against the combined energetic cost of GB and intermetallic precipitate formation. The results shed light on the general trends in the segregation of solutes across the periodic table at GBs in Al and may serve as a design tool to tailor polycrystalline alloys with desired properties.

Acknowledgements

The authors would like to acknowledge financial support from the Australian Research Council (ARC) for funding this work via the ARC Discovery grants scheme (DP150103290). N. Stanford and R. Mahjoub would like to thank Prof. Emily Hilder and Prof. Tanya Monro for their continued support. Computational resources were provided by Intersect Australia Ltd and the computation was undertaken on the NCI National Facility in Canberra, Australia, which is supported by the Australian Commonwealth Government.

References

[1] D. Laughlin, Physical Metallurgy, Elsevier, Amsterdam, 2014.

[2] N.W. Ashcraft, N.D. Mermin, Solid State Physics, Harcourt, Orlando, 1976.

[3] A.P. Sutton, R.W. Balluffi, Interfaces in crystalline materials, Oxford University Press, New York, 1996.

[4] P. Lejcek, Grain Boundary segregaion in metals, Springer, Berlin, 2010.

[5] M.E. Glicksman, Analysis of 3-D network structures, Philos. Mag., 85 (2005) 3-31.

[6] D. Raabe, M. Herbig, S. Sandlobes, Y. Li, D. Tytko, M. Kuzmina, D. Ponge, P.P. Choi, Grain boundary segregation engineering in metallic alloys: A pathway to the design of interfaces, Current Opinion in Solid State & Mater. Sci., 18 (2014) 253-261.

[7] Z.Y. Yu, P.R. Cantwell, Q. Gao, D. Yin, Y.Y. Zhang, N.X. Zhou, G.S. Rohrer, M. Widom, J. Luo, M.P. Harmer, Segregation-induced ordered superstructures at general grain boundaries in a nickel-bismuth alloy, Science, 358 (2017) 97.

[8] R. Kirchheim, Reducing grain boundary, dislocation line and vacancy formation energies by solute segregation. I. Theoretical background, Acta Mater., 55 (2007) 5129-5138.

[9] M. Ferry, N.E. Hamilton, F.J. Humphreys, Continuous and discontinuous grain coarsening in a fine-grained particle-containing Al-Sc alloy, Acta Mater., 53 (2005) 1097-1109.

[10] R. Kirchheim, Grain coarsening inhibited by solute segregation, Acta Mater., 50 (2002) 413-419.

[11] S.J. Zhang, O.Y. Kontsevoi, A.J. Freeman, G.B. Olson, First principles investigation of zinc-induced embrittlement in an aluminum grain boundary, Acta Mater., 59 (2011) 6155-6167.

[12] P. Lejcek, M. Sob, V. Paidar, Interfacial segregation and grain boundary embrittlement: An overview and critical assessment of experimental data and calculated results, Prog. Mater. Sci., 87 (2017) 83-139.

[13] F. Tang, D.S. Gianola, M.P. Moody, K.J. Hemker, J.M. Cairney, Observations of grain boundary impurities in nanocrystalline Al and their influence on micro structural stability and mechanical behaviour, Acta Mater., 60 (2012) 1038-1047.

[14] W. G., Physical metallurgy of nanocrystalline metals, Elsevier, Amsterdam, 2014.

[15] B.K. VanLeeuwen, K.A. Darling, C.C. Koch, R.O. Scattergood, B.G. Butler, Thermal stability of nanocrystalline Pd81Zr19, Acta Mater., 58 (2010) 4292-4297.

[16] S.Y. Ruan, K.L. Torres, G.B. Thompson, C.A. Schuh, Gallium-enhanced phase contrast in atom probe tomography of nanocrystalline and amorphous Al-Mn alloys, Ultramicroscopy, 111 (2011) 1062-1072.

[17] W. Sigle, G. Richter, M. Ruhle, S. Schmidt, Insight into the atomic-scale mechanism of liquid metal embrittlement, Appl. Phys. Lett., 89 (2006).

[18] S.J. Zhang, O.Y. Kontsevoi, A.J. Freeman, G.B. Olson, Sodium-induced embrittlement of an aluminum grain boundary, Phys. Rev. B, 82 (2010).

[19] D.D. Zhao, O.M. Lovvik, K. Marthinsen, Y.J. Li, Segregation of Mg, Cu and their effects on the strength of Al Sigma 5 (210) 001 symmetrical tilt grain boundary, Acta Mater., 145 (2018) 235-246.

[20] X.B. Wu, Y.W. You, X.S. Kong, J.L. Chen, G.N. Luo, G.H. Lu, C.S. Liu, Z.G. Wang, First-principles determination of grain boundary strengthening in tungsten: Dependence on grain boundary structure and metallic radius of solute, Acta Mater., 120 (2016) 315-326.

[21] R.P. Messmer, C.L. Briant, The role of chemical bonding in grain boundary embrittlement, Acta Metall., 30 (1982) 457-467.

[22] W.T. Geng, A.J. Freeman, G.B. Olson, Influence of alloying additions on grain boundary cohesion of transition metals: First-principles determination and its phenomenological extension, Phys. Rev. B, 63 (2001).

[23] D. Ma, M. Friak, J. von Pezold, J. Neugebauer, D. Raabe, Ab initio study of compositional trends in solid solution strengthening in metals with low Peierls stresses, Acta Mater., 98 (2015) 367-376.

[24] D.M. Saylor, B.S. El Dasher, A.D. Rollett, G.S. Rohrer, Distribution of grain boundaries in aluminum as a function of five macroscopic parameters, Acta Mater., 52 (2004) 3649-3655.

[25] A.P. Sutton, R.W. Balluffi, On geometric criteria for low interfacial energy, Acta Metall., 35 (1987) 2177-2201.

[26] R. Dronskowski, P.E. Blochl, Crsytal orbital Hamiltonian populations (COHP) - Energy-resolved visualizaton of chemical bonding in solids based on density functional calculations, J. Phys. Chem., 97 (1993) 8617-8624.

[27] V.L. Deringer, A.L. Tchougreeff, R. Dronskowski, Crystal Orbital Hamilton Population (COHP) Analysis As Projected from Plane-Wave Basis Sets, J. Phys. Chem. A, 115 (2011) 5461-5466.

[28] S. Maintz, V.L. Deringer, A.L. Tchougreeff, R. Dronskowski, Analytic Projection From Plane-Wave and PAW Wavefunctions and Application to Chemical-Bonding Analysis in Solids, J. Comput. Chem., 34 (2013) 2557-2567.

[29] S. Maintz, V.L. Deringer, A.L. Tchougreeff, R. Dronskowski, LOBSTER: A Tool to Extract Chemical Bonding from Plane-Wave Based DFT, J. Comput. Chem., 37 (2016) 1030-1035.

[30] R. Dronskowski, Computational Chemistry of Solid State Materials, Wiley, Weinheim, 2005.

[31] G. Kresse, J. Furthmuller, Efficient iterative schemes for ab initio total-energy calculations using a plane-wave basis set, Phys. Rev. B, 54 (1996) 11169-11186.

[32] G. Kresse, D. Joubert, From ultrasoft pseudopotentials to the projector augmented-wave method, Physical Review B, 59 (1999) 1758-1775.

[33] J.P. Perdew, K. Burke, M. Ernzerhof, Generalized gradient approximation made simple, Phys. Rev. Lett., 77 (1996) 3865-3868.

[34] K. Momma, F. Izumi, Vesta 3 for three-dimensional visualization of crystal, volumetric and morphology data, Journal of Appl. Crystallography, 44 (2011) 24.

[35] D. Scheiber, R. Pippan, P. Puschnig, L. Romaner, Ab initio calculations of grain boundaries in bcc metals, Modelling and Simulation in Materials Science and Engineering, 24 (2016).

[36] D. Scheiber, R. Pippan, P. Puschnig, L. Romaner, Ab initio search for cohesion-enhancing impurity elements at grain boundaries in molybdenum and tungsten, Modelling and Simulation in Materials Science and Engineering, 24 (2016).

[37] V.I. Razumovskiy, A.Y. Lozovoi, I.M. Razumovskii, First-principles-aided design of a new Ni-base superalloy: Influence of transition metal alloying elements on grain boundary and bulk cohesion, Acta Mater., 82 (2015) 369-377.

[38] H. Liu, Y. Gao, J.Z. Liu, Y.M. Zhu, Y. Wang, J.F. Nie, A simulation study of the shape of beta ' precipitates in Mg-Y and Mg-Gd alloys, Acta Mater., 61 (2013) 453-466.

[39] R. Mahjoub, W.Q. Xu, K.J. Laws, M. Ferry, Ab initio study of the likely orientation relationships of interphase and homophase interfaces in a two-phase HCP plus BCC Mg-Li alloy, Comput. Mater. Sci., 139 (2017) 406-411.

[40] S.B. Sinnott, E.C. Dickey, Ceramic/metal interface structures and their relationship to atomic- and meso-scale properties, Materials Science & Engineering R-Reports, 43 (2003) 1-59.

[41] S. Lu, Q.M. Hu, M.P.J. Punkkinen, B. Johansson, L. Vitos, First-principles study of fcc-Ag/bcc-Fe interfaces, Phys. Rev. B, 87 (2013).

[42] J.R. Rice, J.S. Wang, Embrittlement of interfaces by solute segregation, Materials Science and Engineering a-Structural Materials Properties Microstructure and Processing, 107 (1989) 23-40.

[43] C.H. Rycroft, G.S. Grest, J.W. Landry, M.Z. Bazant, Analysis of granular flow in a pebble-bed nuclear reactor, Phys. Rev. E, 74 (2006).

[44] T. Tsuru, H. Somekawa, D.C. Chrzan, Interfacial segregation and fracture in Mg-based binary alloys: Experimental and first-principles perspective, Acta Mater., 151 (2018) 78-86.

[45] G.A. Landrum, R. Dronskowski, The orbital origins of magnetism: From atoms to molecules to ferromagnetic alloys, Angewandte Chemie-International Edition, 39 (2000) 1560-1585.

[46] L.F. Huang, B. Grabowski, J. Zhang, M.J. Lai, C.C. Tasan, S. Sandlobes, D. Raabe, J. Neugebauer, From electronic structure to phase diagrams: A bottom-up approach to understand the stability of titanium-transition metal alloys, Acta Mater., 113 (2016) 311-319.

[47] R. Mahjoub, K.J. Laws, M. Ferry, Amorphous phase stability and the interplay between electronic structure and topology, Acta Mater., 131 (2017) 131-140.

[48] M.A. Gibson, C.A. Schuh, Segregation-induced changes in grain boundary cohesion and embrittlement in binary alloys, Acta Mater., 95 (2015) 145-155.

[49] J. Weissmuller, Alloy thermodynamics in nanostructures, J. Mater. Res., 9 (1994) 4-7.

[50] T. Chookajorn, H.A. Murdoch, C.A. Schuh, Design of Stable Nanocrystalline Alloys, Science, 337 (2012) 951-954.

[51] A.R. Kalidindi, C.A. Schuh, Stability criteria for nanocrystalline alloys, Acta Mater., 132 (2017) 128-137.

[52] P. Lejcek, L. Zheng, S. Hofmann, M. Sob, Applied Thermodynamics: Grain Boundary Segregation, Entropy, 16 (2014) 1462-1483.

[53] J.E. Saal, S. Kirklin, M. Aykol, B. Meredig, C. Wolverton, Materials Design and Discovery with High-Throughput Density Functional Theory: The Open Quantum Materials Database (OQMD), Jom, 65 (2013) 1501-1509.

[54] D.M. Saylor, A. Morawiec, G.S. Rohrer, Distribution of grain boundaries in magnesia as a function of five macroscopic parameters, Acta Mater., 51 (2003) 3663-3674.

[55] D.M. Saylor, A. Morawiec, G.S. Rohrer, The relative free energies of grain boundaries in magnesia as a function of five macroscopic parameters, Acta Mater., 51 (2003) 3675-3686.

[56] D.A. Porter, K.E. Easterling, M.Y. Sherif, Phase Transofrmations in Metals and Alloys, third ed., Taylor & Rrancis Group, Boca Raton, 2009.

TABLE CAPTIONS

Table 1: Symmetric tilt grain boundaries (STGB) along with misorientation angles (degrees), number of atoms in the supercell, supercell dimensions (A°), grain boundary energy (J/m^2) and work of separation (J/m^2). STGBs are presented in coincidence site lattice (CSL) notation where Σ represents density followed by tilt axis and grain boundary orientation.

Grain boundary	θ	# of atoms	Cell dimensions	Υ_{GB}	W_{sep}
Σ3[110](111)	70.5	62	4.946 × 2.856 × 81.589	0.014	1.658
Σ3[110](112)	109.5	85	6.996 × 2.856 × 87.244	0.527	1.400
Σ5[001](210)	53.1	162	9.031 × 4.039 × 84.821	0.497	1.493
Σ5[001](310)	36.9	121	6.386 × 4.039 × 90.879	0.754	1.280
Σ9[110](221)	38.9	109	8.568 × 2.856 × 86.436	0.6464	1.3027
Σ11[110](113)	129.5	134	9.4725 × 2.856 × 94.514	0.1606	1.9883
Σ13[001](320)	67.4	262	14.562 × 4.039 × 86.436	0.7635	1.1267
Σ17[100](410)	93.4	342	16.652 × 4.039 × 96.534	0.7648	1.1221
Σ17[110](223)	28.1	137	11.771 × 2.856 × 80.782	0.4060	1.4858
Σ19[110](331)	26.5	154	12.449 × 2.856 × 84.013	0.4621	1.5307
Σ27[110](115)	148.4	218	14.838 × 2.856 × 97.3423	0.5913	1.5706
Σ43[110](335)	99.4	222	18.731 × 2.856 × 81.2667	0.6354	1.9730

Table 1

FIGURE CAPTIONS

Figure 1: Segregation energy landscape of: (a) group II, III and IV, (b) 3d transition metals and (c) 4d transition metals segregating to twelve GBs and up to four atomic layers next to GBs. The mean of segregation energies for each solute is plotted by the symbol X and the broken red line connecting these symbols is drawn as guide to the eye.

Figure 2: Embrittling potency landscape of: (a) group II, III and IV, (b) 3d transition metal and (c) 4d transition metal solute atoms segregated to different positions at, or in the vicinity, of twelve different symmetric tilt GBs. The mean of embrittling potencies for each solute is plotted by the symbol X and the broken red line connecting these symbols is drawn as guide to the eye.

Figure 3: Volume of Voronoi cell surrounding (a) group II, III and IV solutes and (b) TM segregants at Σ5[001](210).

Figure 4: (a-b) <-ICOHP> of Al-solute pairs for elements of group II, III, IV and TMs respectively segregated at Σ5[001](210). Segregation energy of solutes of (c) group II, III and IV, (d) 3d-TM and (e) 4d-TM respectively segregating at Σ5[001](210).

Figure 5: (a-e) Charge density of Mg, Sn, Ni, Cu, Pd solutes respectively segregated at Σ5[001](210) [34].

Figure 6: (a-b) -ICOHP of Al-Al pairs for segregants of group II, III, IV and TMs respectively. Embrittlement potency of solutes of (c) group II, III and IV, (d) 3d-TM and (e) 4d-TM respectively segregating at Σ5[001](210).

Figure 7: Stability map for (a) group II (b) group III and IV (c) 3d TMs and (d) 4d TMs as solute atoms segregated at or in the vicinity of twelve different GBs. (e-f) Formation energies of second phase for 3d and 4d TM solutes in Al respectively. Broken lines are drawn as guides to the eye.

Figure 8: Weighted fractions of stable, metastable and unstable segregated STGBs.

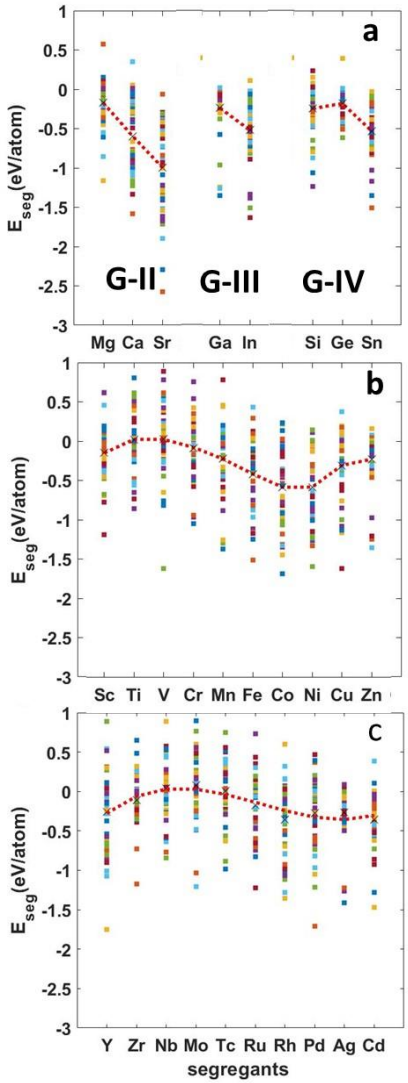

a
b
C
E_{seg}(eV/atom)
1
0.5
0
-0.5
-1
-1.5
-2
-2.5
-3
G-II
G-III
G-IV
Mg Ca Sr Ga In Si Ge Sn
Sc Ti V Cr Mn Fe Co Ni Cu Zn
Y Zr Nb Mo Tc Ru Rh Pd Ag Cd
segregants

Figure 1.

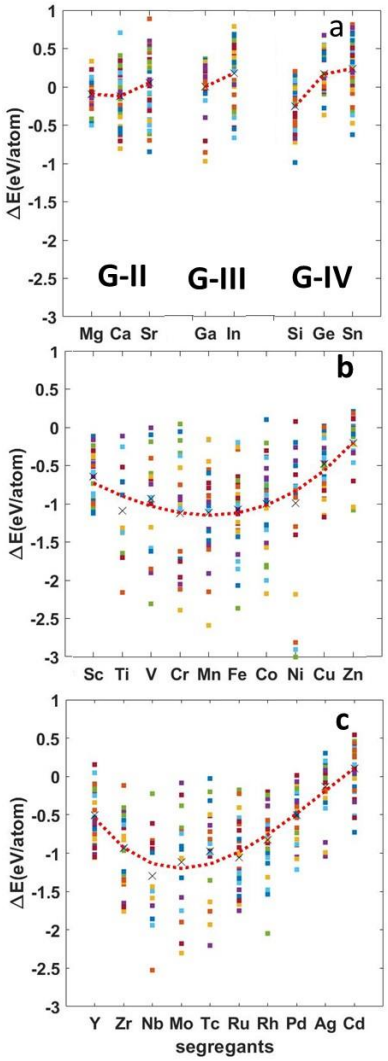

a
b
c
ΔE(eV/atom)
G-II
G-III
G-IV
Mg Ca Sr Ga In Si Ge Sn
Sc Ti V Cr Mn Fe Co Ni Cu Zn
Y Zr Nb Mo Tc Ru Rh Pd Ag Cd
segregants

Figure 2.

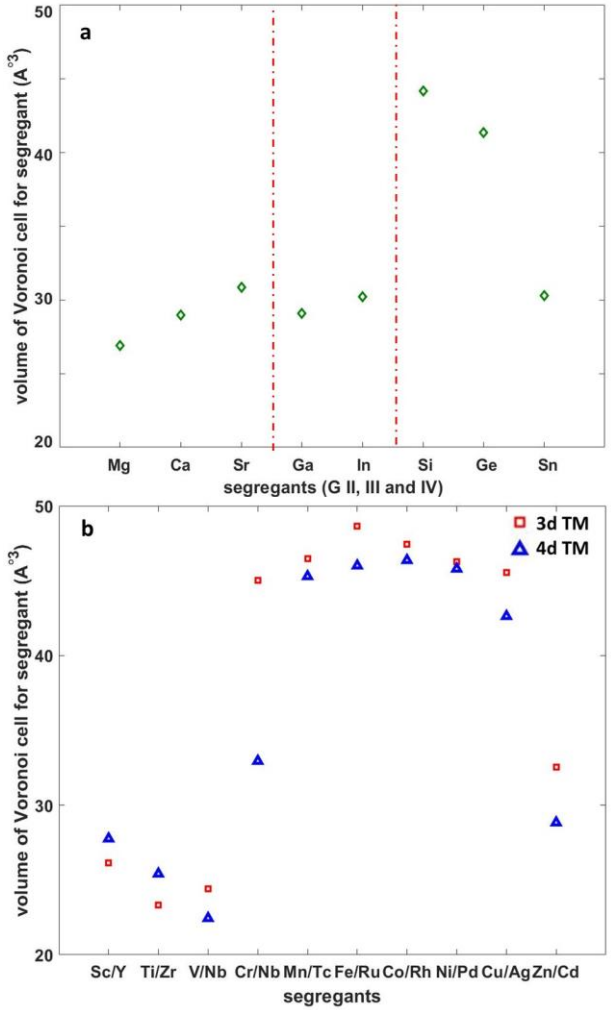

a
volume of Voronoi cell for segregant (A°3)
50
40
30
20
Mg
Ca
Sr
Ga
In
Si
Ge
Sn
segregants (G II, III and IV)
b
3d TM
4d TM
volume of Voronoi cell for segregant (A°3)
50
40
30
20
Sc/Y
Ti/Zr
V/Nb
Cr/Nb
Mn/Tc
Fe/Ru
Co/Rh
Ni/Pd
Cu/Ag
Zn/Cd
segregants

Figure 3.

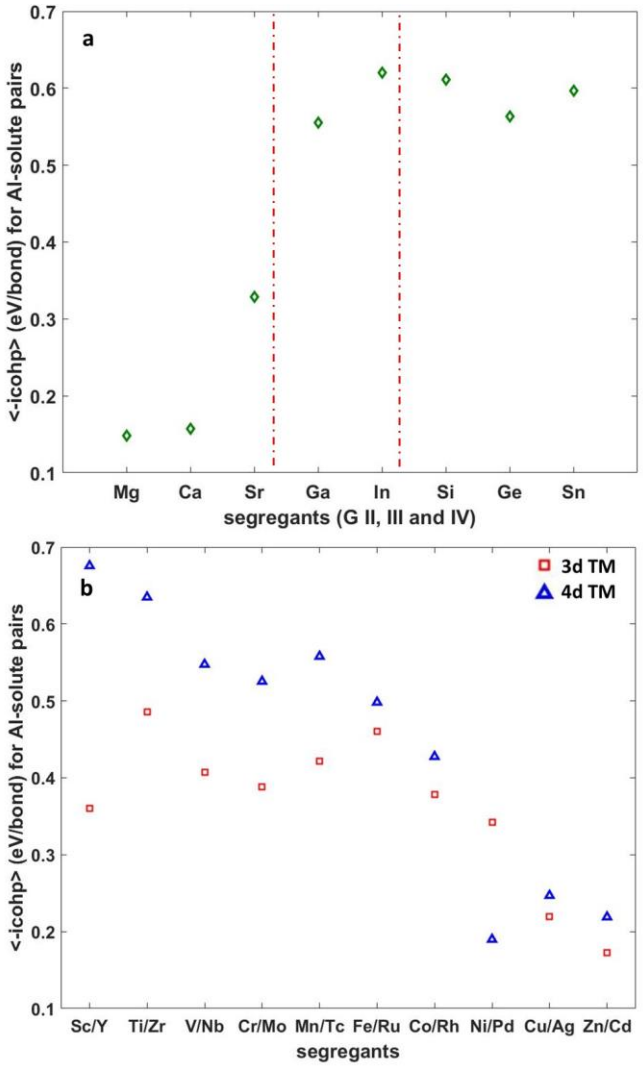

a
<-icohp> (eV/bond) for Al-solute pairs
0.7
0.6
0.5
0.4
0.3
0.2
0.1
Mg
Ca
Sr
Ga
In
Si
Ge
Sn
segregants (G II, III and IV)
b
3d TM
4d TM
<-icohp> (eV/bond) for Al-solute pairs
Sc/Y
Ti/Zr
V/Nb
Cr/Mo
Mn/Tc
Fe/Ru
Co/Rh
Ni/Pd
Cu/Ag
Zn/Cd
segregants

Figure 4(a-b).

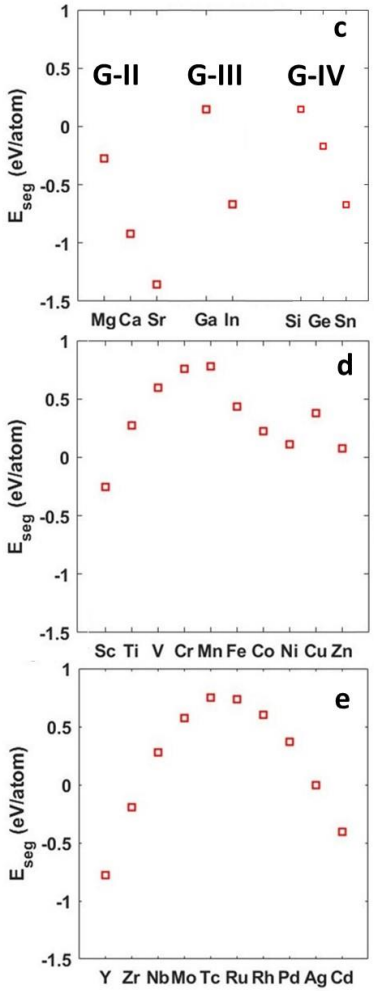

c
G-II
G-III
G-IV
E_{seg} (eV/atom)
1
0.5
0
-0.5
-1
-1.5
Mg Ca Sr Ga In Si Ge Sn
d
Sc Ti V Cr Mn Fe Co Ni Cu Zn
e
Y Zr Nb Mo Tc Ru Rh Pd Ag Cd

Figure 4(c-e).

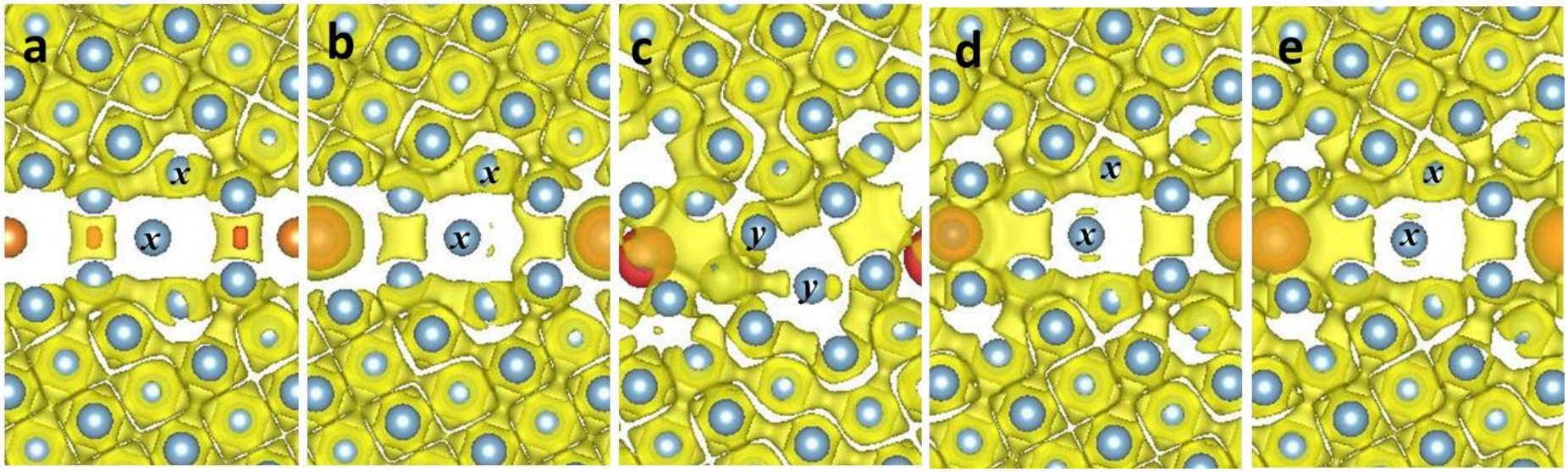


Figure 5.

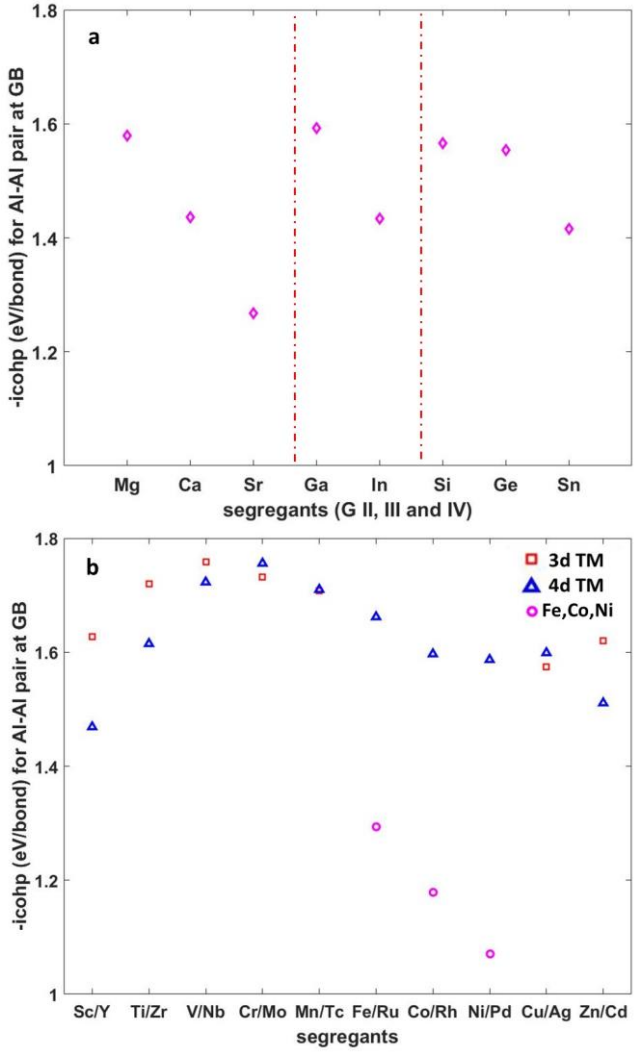

a
-icohp (eV/bond) for Al-Al pair at GB
1.8
1.6
1.4
1.2
1
Mg
Ca
Sr
Ga
In
Si
Ge
Sn
segregants (G II, III and IV)
b
3d TM
4d TM
Fe,Co,Ni
-icohp (eV/bond) for Al-Al pair at GB
Sc/Y
Ti/Zr
V/Nb
Cr/Mo
Mn/Tc
Fe/Ru
Co/Rh
Ni/Pd
Cu/Ag
Zn/Cd
segregants

Figure 6(a-b).

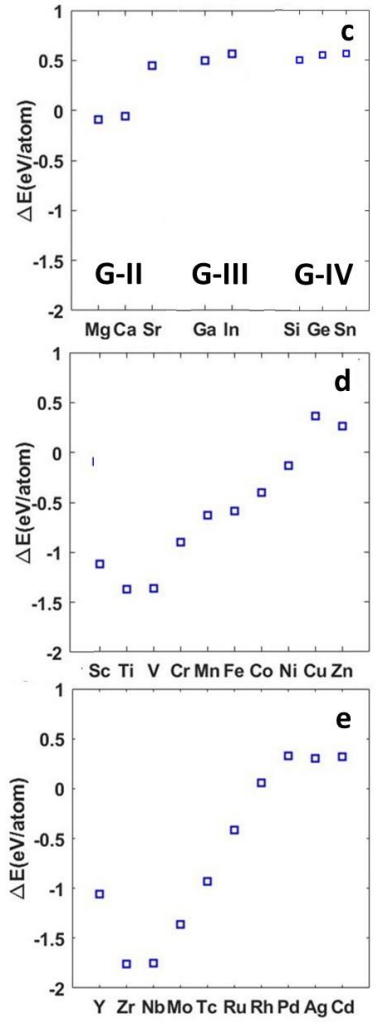

c
ΔE(eV/atom)
G-II
G-III
G-IV
Mg Ca Sr Ga In Si Ge Sn
d
ΔE(eV/atom)
Sc Ti V Cr Mn Fe Co Ni Cu Zn
e
ΔE(eV/atom)
Y Zr Nb Mo Tc Ru Rh Pd Ag Cd

Figure 6(c-e).

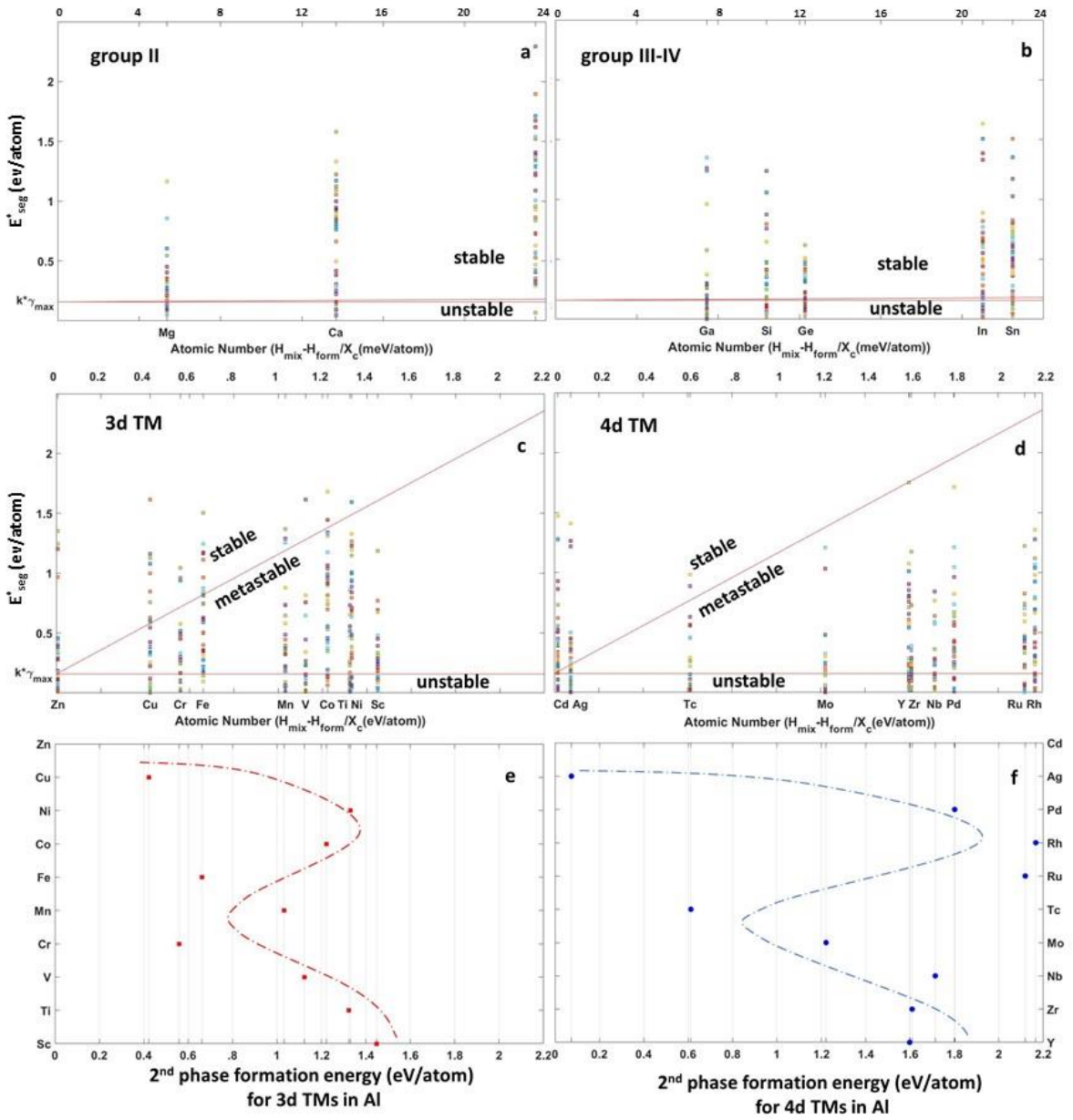

group II
a
group III-IV
b
3d TM
c
4d TM
d
stable
metastable
unstable
E^*_{seg} (ev/atom)
$k^*\gamma_{max}$
Mg
Ca
Ga
Si
Ge
In
Sn
Zn
Cu
Cr
Fe
Mn
V
Co
Ti
Ni
Sc
Cd
Ag
Tc
Mo
Y
Zr
Nb
Pd
Ru
Rh
Atomic Number (H_{mix}-H_{form}/X_c(meV/atom))
Atomic Number (H_{mix}-H_{form}/X_c(eV/atom))
e
f
2nd phase formation energy (eV/atom) for 3d TMs in Al
2nd phase formation energy (eV/atom) for 4d TMs in Al

Figure 7.

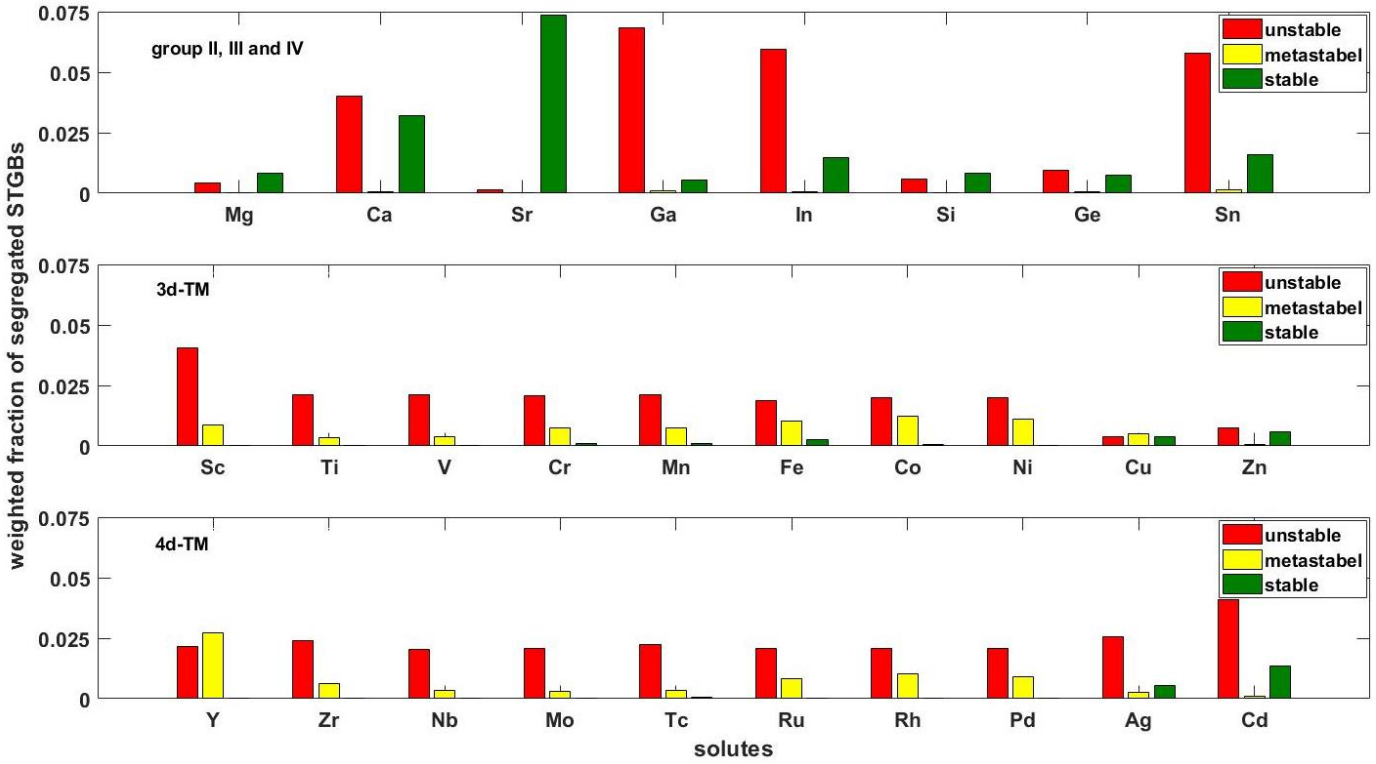


Figure 8.